Retrieval of stratospheric aerosol extinction coefficients from OMPS-LP measurements

Alexei Rozanov[1], Christine Pohl[1], Carlo Arosio[1], Adam Bourassa[2], Klaus Bramstedt[1],
Elizaveta Malinina[1,4], Landon Rieger[2], and John P. Burrows[1]

[1]Institute of Environmental Physics, University of Bremen, Germany
[2]University of Saskatchewan, Canada
[4]now at Canadian Centre for Climate Modeling and Analysis (CCCma), Environment and Climate Change Canada (ECCC), Canada

Correspondence: Alexei Rozanov (alex@iup.physik.uni-bremen.de)

Abstract. A new retrieval algorithm to obtain vertical profiles of the aerosol extinction coefficient from the measurements of the scattered solar light in the limb viewing geometry made by the OMPS-LP instrument is presented. The method employs the normalization of the limb radiances to the solar irradiance in contrast to the normalization by a limb measurement at an upper tangent height, which is used by most of the other published limb-scatter retrievals. The main advantage of this approach is a nearly complete elimination of the dependence of the retrieval results on the prior aerosol extinction profile used in the retrieval. This makes the retrieval well suitable to analyze the observation scenes with highly elevated aerosol plumes as occurred after the Hunga Tonga–Hunga Ha'apai volcanic eruption in January 2022. The results from the new approach were compared to independent data from SAGE III/ISS and OSIRIS. In general, an agreement within 25% between the different data products was observed although larger differences were seen after very strong volcanic eruptions and wildfires. The new data product was used to investigate the evolution of the aerosol plume after the Hunga Tonga–Hunga Ha'apai volcanic eruption.

1 Introduction

Stratospheric aerosols directly influence the radiative budget of the Earth's atmosphere by scattering the incident solar radiation back to the space in the UV-Vis-NIR spectral range and by absorbing the radiation upwelling from the troposphere in the thermal infrared spectral range. As discussed, e.g. by Solomon et al. (2011), the presence of a large amount of aerosols in the stratosphere leads to a global cooling. The cooler temperatures increase the rate of formation of ozone (O_3) (Groves et al., 1978; Groves and Tuck, 1979) and probably decrease the rate of catalytic removal of O_3. In addition, stratospheric aerosols serve as nuclei for the formation of the polar stratospheric clouds (PSCs) or directly provide surface for heterogeneous reactions releasing photo-labile halogens (Cl_2, Br_2 and I_2, but noting that only small amounts of I reach the stratosphere) and inter-halogens (BrCl, ICl and IBr), which are photolyzed and yield halogen atoms. These react with O_3 generating halogen oxides.

Aerosols also take up HNO_3 reducing the amount of NO_x. At sufficiently low NO_x, the ClO disproportionation reaction and the reaction of BrO with ClO participate in additional catalytic cycles, which leads to the formation of the ozone holes in the polar regions (Solomon et al., 1986; Portmann et al., 1996; Tritscher et al., 2021). At high aerosol loading, similar processes might become significant also at extra-polar latitudes, for example, a significant ozone loss was observed in the southern mid-

25 latitudes after the 2020 Australian wildfires and in tropics after the 2022 Hunga Tonga–Hunga Ha'apai eruption (Solomon et al., 2023; Evan et al., 2023). In addition, the global precipitation, sea level pressure and circulation patterns, El Niño and climate extremes were reported to be affected by volcanic eruptions, see e.g. (Fyfe et al., 2013; Khodri et al., 2017; Paik and Min, 2018).

Despite its high scientific importance, the availability of information about the stratospheric aerosols on the global scale is

30 quite limited. One of the widely used characteristics of the stratospheric aerosol, which is available from several space-borne instruments currently in operation, is the stratospheric aerosol extinction coefficient. As discussed by several authors, this quantity can be used to calculate the radiative forcing due to stratospheric aerosols, see e.g. (Hansen et al., 2005; von Savigny et al., 2015; Kloss et al., 2020; Malinina et al., 2021). Global vertical distributions of the stratospheric aerosol extinction coefficient can only be retrieved from space borne measurements. Most robust are the data from solar occultation measurements

35 as performed e.g. by SAGE II (McCormick, 1987) and SAGE III (Chu et al., 1997) instruments, as the corresponding retrievals do not use any strong assumptions in the forward modeling. These data products are well suited for the use as a validation source but suffer from a relatively sparse spatial sampling and coverage. Much more dense spatial sampling is provided by the aerosol extinction data retrieved from measurements of the scattered solar light in limb viewing geometry as done by OSIRIS (Llewellyn et al., 2004), SCIAMACHY (Burrows et al., 1995; Bovensmann et al., 1999) and OMPS-LP (Flynn et al.,

40 2014) instruments. In contrast to the solar occultation measurements, the retrieval of the aerosol extinction coefficients from limb-scatter measurements requires assumptions about the aerosol particle size distribution and aerosol amount around the normalization tangent height, if this kind of the normalization is applied, see e.g. (Rieger et al., 2015). Furthermore, the limb-scatter radiance strongly depends on the reflectance of the troposphere and surface. In the nadir viewing geometry, the aerosol extinction coefficient is retrieved from active remote sensing measurements performed by lidar instruments, such as CALIOP

45 (Winker et al., 2009). Lidar retrievals also employ normalization to measurements at high altitudes resulting in a sensitivity to the aerosol in this range. The major source of uncertainty for lidar instrument is the knowledge of the lidar ratio, see e.g. (Young et al., 2013).

This study focuses on the retrieval of the aerosol extinction coefficient from space borne limb-scatter measurements. Al-though several algorithms to perform such kind of retrievals exist (Bourassa et al., 2012; von Savigny et al., 2015; Rieger

50 et al., 2019; Malinina et al., 2021; Taha et al., 2021; Bourassa et al., 2023) all of them are optimized to mitigate the influence of the surface reflectance and some also minimize error arising from the usage of a fixed aerosol particle size distribution. In this study we present a new algorithm to retrieve vertical distributions of the aerosol extinction coefficient from limb-scatter measurements made by the OMPS-LP instrument. The algorithm has been developed at the University of Bremen. One of its objectives is to minimize the influence of the unknown aerosol loading at high altitudes. This is especially crucial in the

55 case of volcanic eruptions that reach high altitudes, such as the Hunga Tonga–Hunga Ha'apai in January 2022. The latter was

the strongest volcanic eruption in the 21st century with a highest volcanic plume observed in the satellite era and injected a significant amount of SO$_2$ to altitudes up to ∼32 km and a huge amount of the water vapor to altitudes up to ∼50 km, see e.g. (Carr et al., 2022; Legras et al., 2022; Millán et al., 2022; Proud et al., 2022).

Besides the OMPS-LP retrieval developed at the University of Bremen described in this study, algorithms from NASA (Taha et al., 2021) and the University of Saskatchewan (Bourassa et al., 2023) also exist. An intercomparison of the extinction profiles generated by the three algorithms is not straightforward due to the different assumptions about particle size distribution used in the NASA retrieval and the tomographic approach employed in the retrieval developed by the University of Saskatchewan. This intercomparison is a subject of a dedicated study, which is currently ongoing. The CALIOP aerosol extinction profile data (Young et al., 2018) is also available but not used in this study because of very different measurement principle, much smaller footprint in the cross track direction resulting in a significantly sparser coverage, uncertainty from the lidar ratio, and typically low signal to noise ratio in the stratosphere.

The manuscript is structured as follows. In Sect. 2 the observational data used for the retrieval and comparisons are described. Section 3 presents a detailed description of the retrieval algorithm. The selection of the retrieval wavelength is justified in Sect. 4. The main advantages of the new retrieval algorithm are discussed in Sect. 5. Comparisons with independent data are discussed in Sect. 6. Application of the new data set for tracing the evolution of the aerosol plume after the Hunga Tonga–Hunga Ha'apai eruption is presented in Sect. 7. Conclusions are presented in Sect. 8.

2   Measurement data

The Ozone Mapping and Profiler Suite (OMPS) was launched in October 2011 onboard the Suomi NPP satellite of NOAA/-NASA (Flynn et al., 2014). The satellite flies in a sun-synchronous orbit with 98.78° inclination at the altitude of about 800 km. OMPS comprises three instruments: the Nadir Mapper (NM), the Nadir Profiler (NP) and the Limb Profiler (LP). In this study, only the measurements from the latter instrument, OMPS-LP, are used. The OMPS-LP instrument observes solar radiance scattered by the Earth's atmosphere including that passing through the atmosphere downwards and reflected back by the underlying surface. The radiance from the atmosphere enters the instrument through three slits pointing in the direction opposite to that of the satellite's flight. By using two-dimensional charged-coupled device (CCD) detectors, measurements are done simultaneously in the altitude range from approximately 0 to 100 km with a vertical sampling of 1 km. Because of remaining calibration issues, only the measurements from the central slit are used in this study. OMPS-LP instrument is a prism spectrometer covering the 280 - 1000 nm spectral range with a spectral resolution increasing with the wavelength from 1 nm in the UV to about 30 nm in the near-IR region. The vertical field of view of each detector pixel is about 1.5 km. In this study, the Level 1 data V2.6 provided by NASA are used.

The Stratospheric Aerosol and Gas Experiment (SAGE) III instrument has been operating since February 2017 onboard the International Space Station (ISS). The ISS flies at ∼400 km altitude and its orbit has an inclination of 51.6°. SAGE III/ISS instrument performs solar occultation measurements during sunrise and sunset. The aerosol extinction coefficients are provided at 9 wavelengths: 384, 449, 520, 602, 676, 756, 869, 1021, and 1544 nm. The retrievals cover the range from the cloud top

to about 45 km altitude at a vertical resolution of about 0.75 km. In this study Level 2 V5.3 data from the SAGE III/ISS
90   instrument were used. No cloud filtering was applied. Negative values in SAGE III/ISS data were not filtered out to avoid
creating a positive bias.

The Optical Spectrograph and InfraRed Imaging System (OSIRIS) instrument (Llewellyn et al., 2004) was launched in
November 2001 onboard the Swedish Odin satellite. The satellite flies in a sun-synchronous orbit with 98.78° inclination at
the altitude of about 600 km. The instrument combines a grating UV/Vis spectrograph and an IR imager and observes the solar
95   radiance scattered by the Earth's atmosphere including that reflected by the underlying surface. The observations are done in
the altitude range between about 0 and 100 km with a vertical sampling of ∼2 km and similar vertical resolution. The optical
spectrograph, whose data were used in this study, measures the spectral radiance in the 280–800 nm range with a resolution of
1–2 nm. OSIRIS retrieval provides vertical profiles of the stratospheric aerosol extinction coefficient at a wavelength of 750 nm
between about 8 and 40 km with a vertical resolution of about 2 km. In this study, OSIRIS cloud cleared Level 2 data of V7.3
100 were used (Rieger et al., 2019). Because of issues identified by the University of Saskatchewan team in the vertical profiles of
the aerosol extinction coefficient retrieved after the Hunga Tonga–Hunga Ha'apai eruption, only data before January 2022 are
considered.

3   Retrieval algorithm

In this section, a detailed description of the new OMPS-LP retrieval algorithm of the University of Bremen (V2.1) is presented.
105 The retrieval approach is based on a regularized non-linear inversion. In general, the following quadratic form needs to be
minimized to obtain the solution:

$$\| \, y - F(x_o) - K(x - x_0) \, \|_{S_y^{-1}} + \| \, x - x_0 \, \|_{S_r} \, , \tag{1}$$

where x is the resulting state vector, i.e. the solution to be obtained, x_0 is the initial guess state vector, $K = \frac{\delta F(x)}{\delta x}\Big|_{x=x_0}$ is the
Jacobian of the forward model operator also referred to as the weighting function, y is the measurement vector constructed from
110 the observed values, $F(x_0)$ is the measurement vector simulated by the forward model assuming the initial guess atmospheric
state, S_y^{-1} is the noise covariance matrix and S_r is the regularization matrix.

The state vector contains aerosol extinction coefficient values at altitude levels corresponding to the measurement tangent
heights and the effective Lambertian surface albedo. The initial guess values for the aerosol profile are set in accordance with
an arbitrary profile extracted from the SAGE II aerosol climatology published by Bingen et al. (2004). As the retrieval depends
115 only weakly on the initial guess profile (see below), selection of any particular profile is rather unimportant. For the effective
surface albedo, the initial guess value is set to 0.5. The initial guess state vector is the same for all retrievals. The aerosol
extinction coefficient and the scattering phase function are calculated employing Mie theory. We assume that a) the aerosol
consists of spherical droplets made of 75% H_2SO_4, b) the relative humidity of the ambient air is 0%, and c) the droplets have a
unimodal log-normal particle size distribution (PSD) with fixed parameters (median radius, R_{med}, of 0.08 μm and geometrical
120 standard deviation, σ, of 1.6). The latter are taken from an arbitrary balloon-borne in-situ measurement for background aerosol

conditions reported by Deshler (2008). An aerosol layer between 0 and 50 km and an aerosol free atmosphere above are assumed.

The measurement vector contains logarithms of the limb radiance in the tangent height range 8.5 – 48.5 km (with 1 km sampling) normalized by the solar irradiance. This normalization approach makes the main difference between the new re-trieval and the previous version of the OMPS-LP retrieval of the University of Bremen (V1.0.9) published by Malinina et al. (2021), where the normalization used a limb measurement at an upper tangent height. As the normalization by the solar irra-diance makes the retrievals more sensitive to the surface reflectance, the approach to retrieve the effective Lambertian surface albedo was optimized as follows. In the new retrieval, the effective surface albedo is included in the state vector and retrieved simultaneously with the aerosol extinction coefficients. Measurements at all tangent heights in 8.5 – 48.5 km range are used to retrieve the effective surface albedo. In contrast, the V1.0.9 approach performed alternating independent retrievals of the aerosol extinction coefficients and of the effective surface albedo. The latter retrieval used only the limb measurement at the reference tangent height. In addition, V2.1 approach is more sensitive to the quality of the radiative transfer modeling. For this reason, the fully spherical mode of the SCIATRAN radiative transfer model (Combined Differential-Integral approach involving the Picard Iterative approximation, CDIPI) was used for the forward modeling rather than the approximate spherical mode (Combined Differential-Integral approach, CDI) used in V1.0.9 algorithm. A detailed description of the CDI and CDIPI modes of SCIATRAN can be found in (Rozanov et al., 2000, 2001). We note that the use of the solar normalization makes the retrieval more sensitive to the quality of the absolute calibration of the measurements. In particular, an error can be expected if the absolute calibration of the limb spectra and that of the solar irradiance spectra differ. Although absolute calibration errors are typically independent of the incoming signal, they might be differently re-distributed by the retrieval between the retrieved parameters (aerosol extinction coefficient and effective surface albedo in our case) depending on the observational geometry and surface reflectivity. This makes them difficult to be identified. In a case of a degradation of the detector a drift in the data might be expected. A degradation of detectors is, however, more an issue in the UV spectral range rather than in near-IR used in this study. For now, no indications for any issues in the absolute calibration of OMPS-LP instrument or degradation of the detectors are identified.

The retrieval is done for the relative changes in the aerosol extinction coefficient, $([x]_i - [x_0]_i)/[x_0]_i$, and absolute changes in the effective surface albedo, $[x]_j - [x_0]_j$. In the formulas above, the square brackets denote the componentwise operation, i runs through all aerosol levels included into the retrieval and j is the number of the effective surface albedo component in the state vector. The regularization is based on the Tikhonov approach with zeroth and first order terms:

$$S_r = S_a^{-1} + \gamma^{-2} S_d^T S_d. \tag{2}$$

The zeroth order Tikhonov term, S_a^{-1}, acts in a similar way as the a priori covariance matrix in the maximum a posteriori method described by Rodgers (2000). The diagonal elements of the matrix S_a are set to 0.3 for the aerosol extinction coeffi-cients and to 0.01 for the effective surface albedo. The off-diagonal elements are selected assuming a 1 km correlation radius for the aerosol extinction coefficients and no correlation between the aerosol extinction and the effective surface albedo. The matrix S_d in the first order Tikhonov term is the first derivative matrix. Detailed formulas to calculate the elements of the

Table 1. Retrieval settings in OMPS-LP V2.1 and V1.0.9 algorithms of the University of Bremen.

	Old retrieval version: V1.0.9	New retrieval version: V2.1
Retrieval wavelength	869 nm	869 nm
Tangent height range	12.5 – 37.5 km	8.5 – 48.5 km
Normalization approach	Limb measurement at the normalization tangent height (37.5 km)	Solar irradiance
Retrieval approach	Regularized non-linear inversion	Regularized non-linear inversion using Levenberg-Marquardt approach
Regularization	Zeroth and first order Tikhonov regularization w.r.t. the solution at a previous iterative step	Zeroth and first order Tikhonov regularization w.r.t. the solution at a previous iterative step
Radiative transfer model	SCIATRAN, approximate spherical mode	SCIATRAN, full spherical mode
Assumed aerosol layer	12 – 45 km	0 – 50 km
Assumed aerosol PSD	unimodal log-normal distribution, fixed parameters: $R_{med} = 0.08\ \mu$m, $\sigma = 1.6$	unimodal log-normal distribution, fixed parameters: $R_{med} = 0.08\ \mu$m, $\sigma = 1.6$
Aerosol/albedo retrieval	Independent at each step, alternated	Joint, simultaneous
Measurements used for the surface albedo retrieval	Limb measurement at the normalization tangent height (37.5 km)	All tangent heights included in the retrieval (8.5 – 48.5 km)

155 regularization matrices can be found in (Rozanov et al., 2011). The Tikhonov parameter, γ, is set to 0.2. The noise covariance matrix is a diagonal matrix with diagonal elements corresponding to a signal-to-noise ratio of 200, independent of the tangent height. This value as well as the values of Tikhonov parameters were selected empirically as a trade-off between the stability and sensitivity of the retrievals. Taking into account that the regularization strength is determined by the ratio of the noise covariance and Tikhonov parameters rather then their absolute values, we prefer to use an empirical value for the signal-to-noise

160 ratio rather than the reported measurement errors. This keeps the regularization strength similar for all retrievals.

The non-linearity of the inverse problem defined by Eq. 1 is accounted for by employing an iterative scheme. The Levenberg-Marquardt algorithm is used to obtain the final solution. At each iterative step, the solution of the non-linear inverse problem is written as (see, e.g. (Rodgers, 2000) for details):

$$x_{i+1} = x_i + \left[K_i^T S_y^{-1} K_i + S_r + \lambda S_a^{-1} \right]^{-1} K_i^T S_y^{-1} \left(y - F(x_i) \right), \tag{3}$$

165 where i is the iteration number and λ in the Levenberg-Marquardt parameter with an initial guess of 1. We note that the regularization is done with respect to the solution at the previous iterative step rather than with respect to the initial guess atmospheric state. With that, a constraint to the magnitude and shape of the difference profile is applied only within a single iterative step making the difference between the final solution and the initial guess state much less constrained. The iterative process stops if the aerosol extinction coefficient at two subsequent iterative steps does not change by more than 2% between

170 15 and 28 km or if the relative change in the total root mean square difference is below 0.001. The convergence criteria are selected empirically taking into account the targeted precision of the retrieved aerosol extinction profiles of about 10%. The results are rejected if the retrieval requires more than 100 iterations to converge. The averaging kernels, which describe the
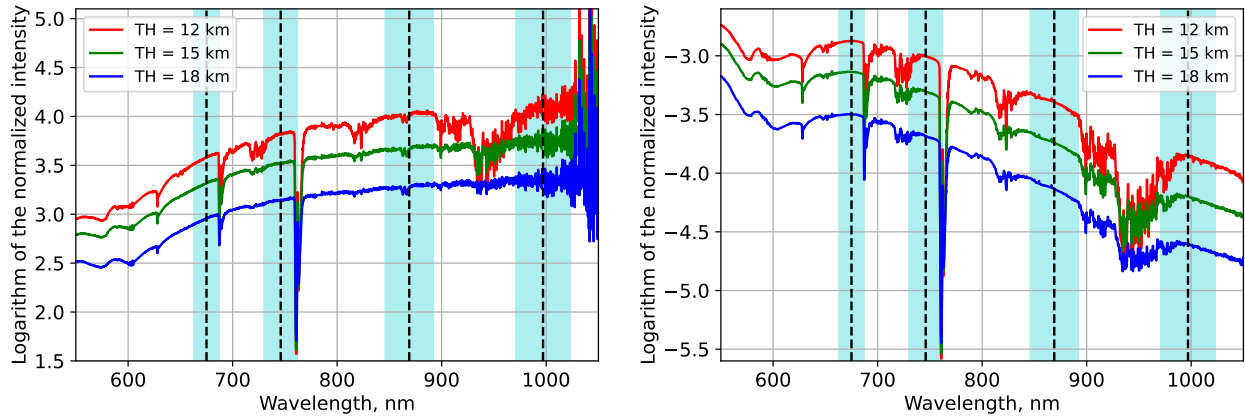
Figure 1. Spectra of limb-scatter radiance at different tangent heights normalized by the limb measurement at the reference tangent height (left panel) and by the solar irradiance spectrum (right panel). Dashed lines depict selected central wavelengths used by the NASA aerosol retrieval (675, 745, 869 and 997 nm). The cyan shadings mark ranges of ± FWHM of the OMPS-LP instrument around the central wavelengths of the NASA aerosol retrieval.

sensitivity of the retrieval to the true state, are calculated at the last (n-th) iteration by using the following formula:

$$A = \left[K_{n-1}^T S_y^{-1} K_{n-1} + S_r + \lambda S_a^{-1} \right]^{-1} K_{n-1}^T S_y^{-1} K_{n-1}. \tag{4}$$

175   The most important settings used in the new OMPS-LP retrieval approach of the University of Bremen (V2.1) and those of its precursor version (V1.0.9) are summarized in Table 1.

4   Optimization of the retrieval wavelength

The optimal wavelength for the OMPS-LP V2.1 aerosol retrieval of the University of Bremen is selected by (i) analyzing possible contamination of the measured signal by interfering spectral signatures of other atmospheric constituents and (ii) 180   investigating the sensitivity of limb-scatter measurements to the vertical distribution of the stratospheric aerosol.

To investigate potential influence of interfering absorbers, a measured or modeled atmospheric spectrum, which has higher spectral resolution and sampling than that of OMPS-LP, is required. To ensure that all relevant spectral signatures from all atmospheric constituents are taken into account and their strength is representative for real observational conditions, we decided to analyze a measured spectrum rather than the modeled one. A suitable spectral information was provided by the SCIA-185   MACHY spectrometer, which flew onboard the European Envisat satellite from March 2002 to April 2012 and had a similar observational geometry to that of the OMPS-LP instrument. While the most recent version of the University Bremen retrieval described in this study uses the sun-normalized limb-scatter measurements, all previous retrieval versions as well as most of the other limb-scatter stratospheric aerosol retrievals use the limb radiances normalized by the limb measurements at an upper

tangent height (also referred to as the reference tangent height). For this reason, below we analyze the spectral behavior of both

190   the sun-normalized and reference tangent height normalized radiance.

Figure 1 shows spectra of the limb-scatter radiance at different tangent heights normalized by the limb measurement at the reference tangent height of 35 km (left panel) and by the solar irradiance spectrum (right panel). The spectra were obtained from the SCIAMACHY measurement performed on January 7th, 2004 at 16:24:37 UTC with tangent point ground coordinates 26°S, 5°W. The vertical dashed lines mark the wavelengths of 675, 745, 869 and 997 nm, which were used by the NASA

195   OMPS-LP V2.0 stratospheric aerosol extinction retrieval (Taha et al., 2021). The cyan shadings mark the areas smeared by the spectral response function (SRF) of the OMPS-LP instruments. The width of the shadings is selected as $\pm$ FWHM (full width at half maximum of the SRF). The latter were estimated from Fig. 1-3 in (Rault et al., 2010) as 12, 16, 23 and 26 nm at 675, 745, 869 and 997 nm, respectively. The figure reveals that the band centered at 675 nm touches at its long-wave edge the O_2-A absorption band centered at 690 nm. A similar situation is observed for 745 nm. At this wavelength, the measurements

200   might be affected by the strong absorption in O_2-B band centered at 762 nm. A potential influence of the ozone absorption is similar for radiances normalized by the measurement at the reference tangent height and by the solar irradiance spectrum. The band centered at 869 nm approaches at its long-wave edge the water vapor absorption band, however the potential interference is rather small. For the reference tangent height normalization a small spectral feature is present in the middle of the band, which is not present for the sun-normalized radiance. This is most probably an emission signature propagating from the

205   measurement at the reference tangent height. At 997 nm, the measurements might be affected by the water vapor absorption at the short-wave edge of the band. This influence seems to be stronger for the sun-normalized radiance. The reason for that is a partial canceling of the tropospheric signal when using the reference tangent height normalization. A strong increase of the measurement noise towards the longer wavelengths in the case of the reference tangent height normalization is typical for SCIAMACHY. For the OMPS-LP instrument, the signal-to-noise ratio at 997 nm is about a factor of two lower than that at 869

210   nm. Because of a stronger overlap with absorption features of atmospheric gases and lower signal-to-noise ratio as compared to other wavelengths, we exclude the 997 nm wavelength from the further consideration.

To investigate the sensitivity of the OMPS-LP V2.1 aerosol retrieval to changes in the vertical distribution of the aerosol extinction coefficient, the averaging kernels (see Eq. 4) at different wavelengths were analyzed for an example OMPS-LP measurement performed on January 6th, 2018 at 15:04:37 UTC with tangent point ground coordinates 51°S, 14°W. The results

215   are presented in Fig. 2. The averaging kernels (AKs) for wavelengths of 675, 745 and 869 nm are presented in the left panel of the plot. For clarity reason, only each third AK between 9.5 and 33.5 km is plotted. It is seen that the AKs for 675 nm (red) are always smaller than those for 745 nm (green) and 869 nm (blue) and significantly degrade below 15 km. This highlights a lower sensitivity of the retrieval at 675 nm with respect to the other two wavelengths at all altitudes. At the lowermost altitude shown in the plot (9.5 km), the AK for 675 nm is very small and its peak is strongly displaced from the nominal altitude, which

220   is an indication of a nearly complete loss of sensitivity below 10 km. Comparing AKs for 745 and 869 nm, we see that the former are only slightly lower than those for 869 nm at almost all altitudes and even slightly higher above 30 km. For both wavelengths, AKs peak at their nominal altitudes.
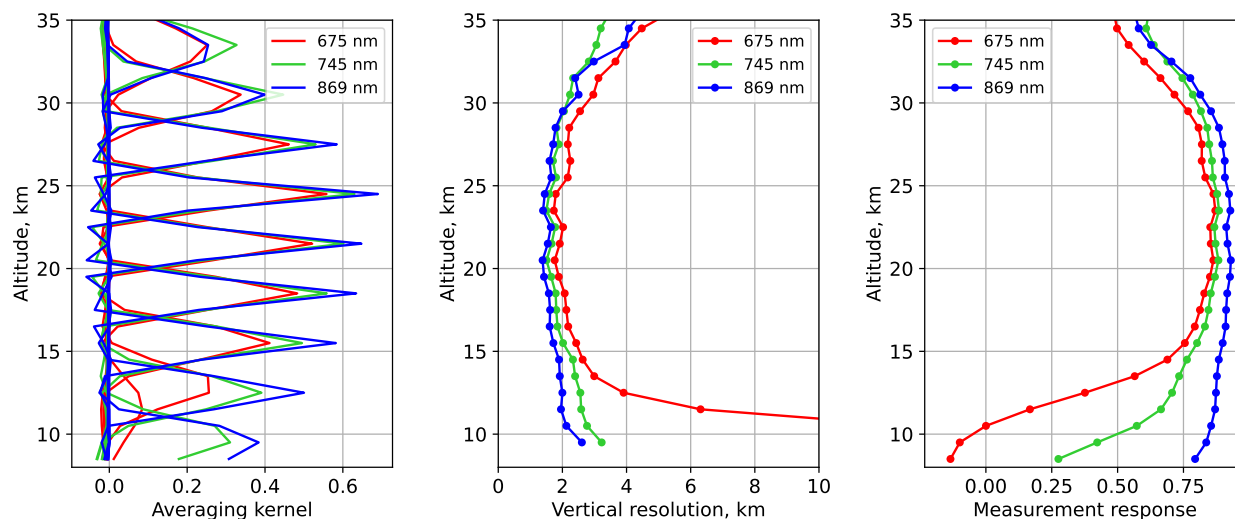
Figure 2. Characteristics of the OMPS-LP V2.1 aerosol extinction coefficient retrieval of the University of Bremen for different wavelengths.
Left panel: averaging kernels. Middle panel: vertical resolution. Right panel: measurement response.

The middle panel of Fig. 2 shows the vertical resolution of the retrieval for different wavelengths. It is calculated as a
reciprocal of the diagonal elements of the AK matrix multiplied by the step of the retrieval vertical grid (1 km in our case).
225 Confirming the conclusions drawn from the left panel of the plot, the vertical resolution of the retrieval at 675 nm is only a bit
lower compared to that at two other wavelengths down to 13.5 km and starts to degrade rapidly below this altitude exceeding
the value of 10 km at 11.5 km altitude level. The vertical resolution of the retrieval at 745 nm is slightly worse than that at
869 nm below 30 km and is slightly better above. A similar behavior is seen for the measurement response shown in the right
panel of Fig. 2 and calculated as a sum of the elements in the AK matrix rows. The measurement response for the retrieval at
230 869 nm is close to the ideal value of one with values better than 0.75 below 31.5 km altitude. At both 675 and 745 nm, the
measurement response starts to degrade at lower altitudes crossing the 0.5 level at about 13 km for the former and about 10 km
for the latter wavelengths.

Based on the discussion in this section we consider the wavelength of 869 nm to be optimal for the retrieval of vertical profiles
of the stratospheric aerosol extinction coefficient from limb-scatter measurements performed by the OMPS-LP instrument.

235 **5   Main advantages of the new retrieval algorithm**

Several advantages are associated with the normalization of the limb radiance by the solar irradiance as it is done in the new
V2.1 retrieval of the University of Bremen with respect to the normalization by the limb measurement at the reference tangent
height as it was done in the precursor V1.0.9 retrieval described by Malinina et al. (2021) and other limb-scatter stratospheric
aerosol retrievals (Bourassa et al., 2008; von Savigny et al., 2015; Taha et al., 2021). First, limb measurements at upper tangent
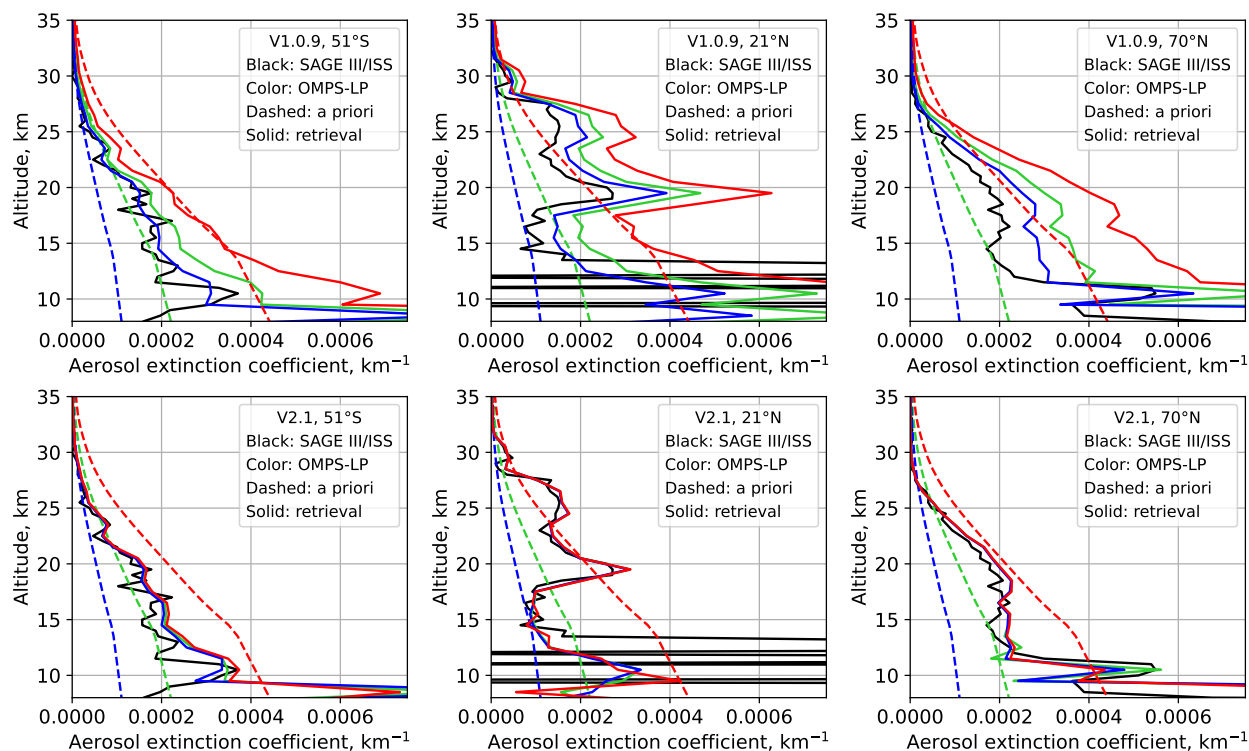
Figure 3. Dependence of the retrieval results on the a priori aerosol extinction profile for the University of Bremen retrievals using the normalization to the limb measurement at the reference tangent height, V1.0.9 (top row), and to the solar irradiance spectrum, V2.1 (bottom row). The comparisons are done for three example OMPS-LP measurements. Left column: January 6, 2018, 15:04:37 UTC; 51°S, 14°W. Middle column: January 22, 2018, 10:20:45 UTC; 22°N, 43°E. Right column: July 25, 2018, 04:39:29 UTC; 70°N, 107°E.

240 heights generally have lower signal to noise ratios and are more contaminated by the stray light as compared to measurements at lower tangent heights. Thus, dividing all measurements by one at an upper tangent height generally degrades the quality of all data used in the retrieval. Second, a presence of an unknown signal from the aerosol scattering at the reference tangent height might bias the retrieval if the a priori aerosol content used in the forward model significantly differs from the real one. In addition, the reference tangent height is often used to estimate the effective Lambertian albedo of the underlying scene and a

245 wrong assumption about the aerosol scattering contribution at this tangent height might bias the retrieved value of the effective albedo, which might additionally bias the retrieved vertical profile of the aerosol extinction coefficient.

The increase of the measurement noise when using the reference tangent height normalization approach is clearly seen in Fig. 1. The spectra in the left panel of the plot are obviously noisier compared to those in the right panel, especially for the longer wavelengths.

250 To illustrate the dependence of the retrievals using different normalization approaches on the a priori aerosol extinction pro-file, we performed retrievals for three example measurements of OMPS-LP using three different a priori profiles: the standard
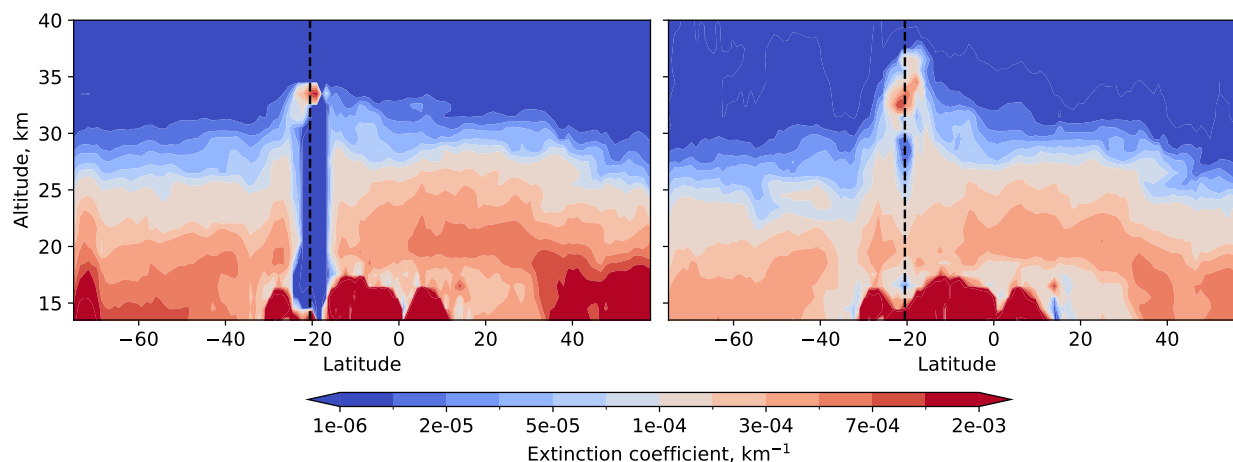
Figure 4. Aerosol extinction coefficient at 869 nm retrieved from OMPS-LP measurements during the orbit 52974 on January 17th, 2022. Left panel: using normalization to the reference tangent height (V1.0.9). Right panel: using normalization to the solar irradiance (V2.1). Dashed lines mark the location of the Hunga Tonga–Hunga Ha'apai volcano.

one, halved for all altitudes and doubled for all altitudes. The results of this investigation are shown in Fig. 3. The plot reveals that the results obtained using the normalization to the reference tangent height (top row) strongly depend on the a priori profile used in the retrieval. We note that the bulk effect comes from the scaling of the a priori profile at the altitude level corresponding

255 to the reference tangent height. In contrast, the retrieval results obtained using the normalization to the solar irradiance (bottom row) are almost independent from the a priori profile. In this case, small deviations between the results obtained for different a priori profiles are only seen below about 12.5 km altitude.

The dependence of the V1.0.9 retrieval on the aerosol amount around the tangent tangent of the reference measurement results in retrieval artifacts if a strong aerosol plume resides in this altitude range. This effect is illustrated in Fig. 4, where

260 retrieval results for an OMPS-LP single orbit shortly after the Hunga Tonga–Hunga Ha'apai eruption (January 2022) are presented. It is seen from the plot that V1.0.9 retrieval (left panel) shows unrealistically low values below the aerosol plume located in the reference tangent height region (38.5 km). As seen from the right panel of the plot, this artifact is not present in the V2.1 retrieval, which uses the normalization to the solar irradiance. There is still a range of quite small values below the aerosol plume seen in the right panel of the plot. For now, we cannot definitely say whether it is a real minimum in the aerosol

265 extinction or a remaining retrieval artifact. It is also seen form the plot that V2.1 retrieval shows generally lower values than V1.0.9. As discussed below, these lower values are in a better agreement with reference measurements highlighting another advantage of the new approach.
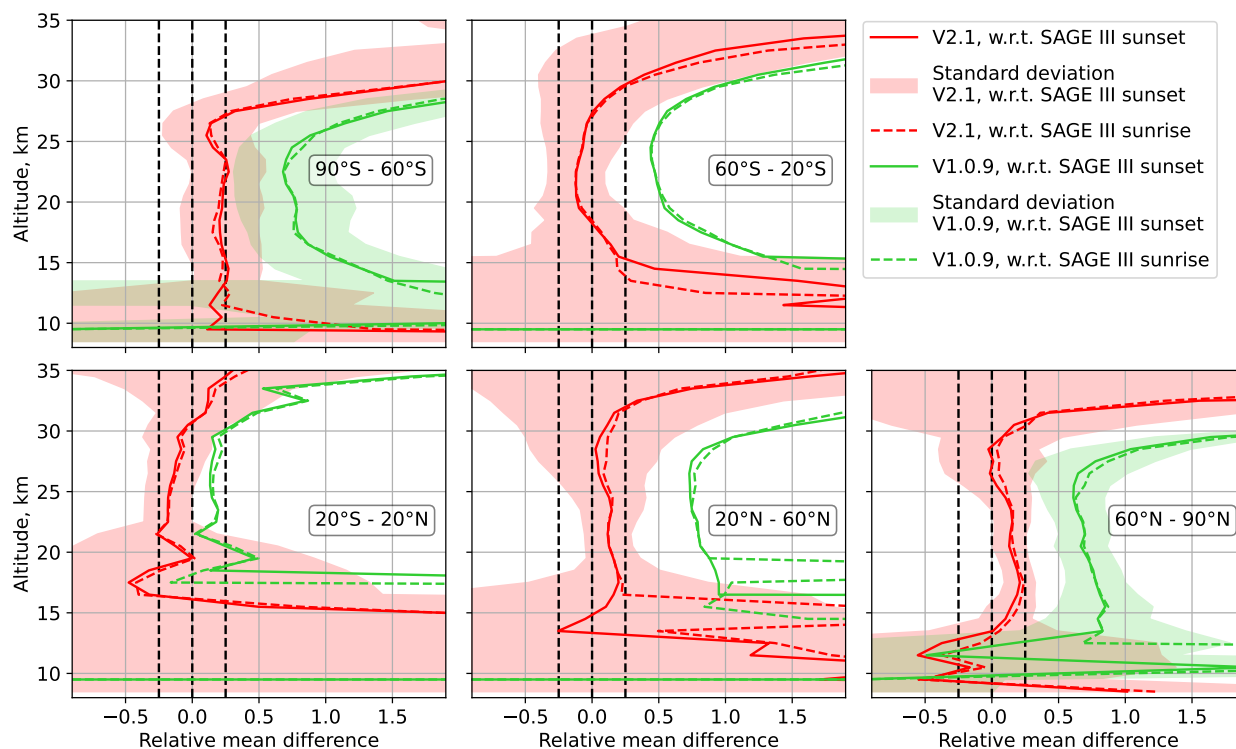
Figure 5. Comparison of V2.1 and V1.0.9 OMPS-LP retrieval results with colocated SAGE III/ISS data for 2018 for different latitude bands. The vertical black dashed lines mark 0% and ±25% levels.

6 Comparison with other datasets

To assess the quality of the new retrieval and demonstrate the achieved improvement, the OMPS-LP results of versions 2.1 and 1.0.9 were compared to the colocated data from SAGE III/ISS. For this comparison no cloud filtering was applied for both data products. The comparison of the aerosol extinction coefficients at 869 nm from both instruments for the year 2018 (arbitrary selected) in different latitude bands is presented in Fig. 5. The relative difference was calculated as (OMPS-LP - SAGE_III)/SAGE_III. The comparisons were done independently for SAGE III/ISS sunset (solid lines) and sunrise (dashed lines) measurements. For reasons of clarity, the standard deviation of the differences is shown only for colocations with the SAGE III/ISS sunset measurements. The plot demonstrates that V2.1 retrieval generally shows lower values than those from V1.0.9 significantly reducing differences to the SAGE III/ISS results for most of the latitude bands. In the tropics, the agreement with SAGE III/ISS data is similar for both V2.1 and V1.0.9 results with differences changing from mostly positive for V1.0.9 to mostly negative for V2.1. Typically, V2.1 OMPS-LP retrieval agrees within 25% with SAGE III/ISS data between 18 and 30 km. Only in high southern latitudes the agreement starts degrading already above 27 km. In the lower stratosphere, a good agreement is seen down to about 13 km in the northern extra-tropics (about 16 km for sunrise colocations in the northern mid-
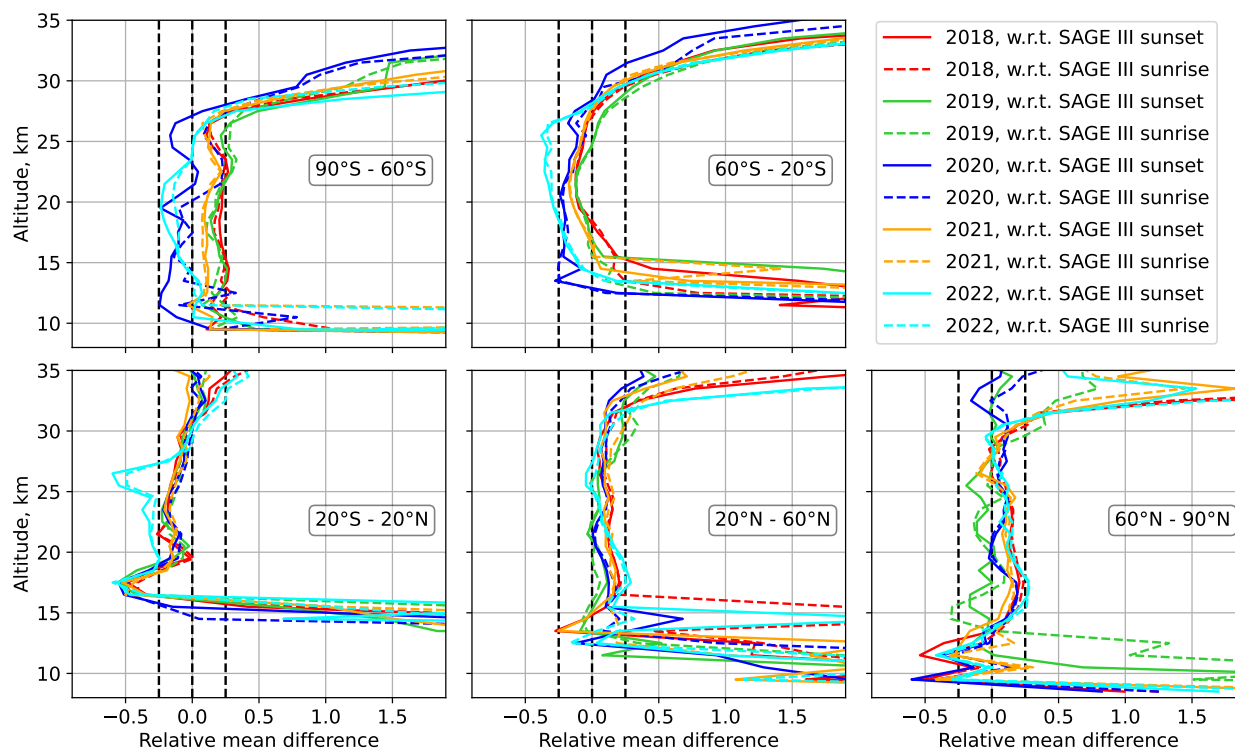
Figure 6. Comparison of V2.1 OMPS-LP retrieval results with colocated SAGE III/ISS data for different years and different latitude bands. The vertical black dashed lines mark 0% and ±25% levels.

latitudes), down to 15 km in the southern mid-latitudes and down to 8(12) km for sunset(sunrise) colocations in the southern high latitudes.

Figure 6 presents relative mean differences between the aerosol extinction coefficients at 869 nm retrieved from OMPS-LP and SAGE III/ISS observations for different years. Here, only V2.1 of OMPS-LP retrieval is shown. The plot reveals that differences between OMPS-LP and SAGE III data are very similar for most of the years and latitude bands. Exceptions are
285 seen for (i) the tropics and southern extra-tropics in 2022, where the influence of the Hunga Tonga–Hunga Ha'apai eruption is the strongest, (ii) the southern extra-tropics in 2020, which is most probably explained by the strong aerosol pollution from Australian wildfires, and (iii) the northern high latitudes in 2019, most probably because of the Raikoke eruption. In general, the differences in the anomalous years are more negative indicating that OMPS-LP V2.1 aerosol extinction product is lower
290 than SAGE III/ISS data in cases of stronger aerosol load in the stratosphere.

To evaluate a time evolution of the stratospheric aerosol extinction coefficients in more details, monthly zonal mean time series from OMPS-LP V2.1 retrievals were compared with the results from SAGE III/ISS and OSIRIS instruments. A rough cloud filtering was done when calculating OMPS-LP V2.1 monthly zonal mean data by rejecting the extinction coefficient values larger than 0.1. To perform the comparison, the OMPS-LP data were converted to the wavelengths of 750 nm using the
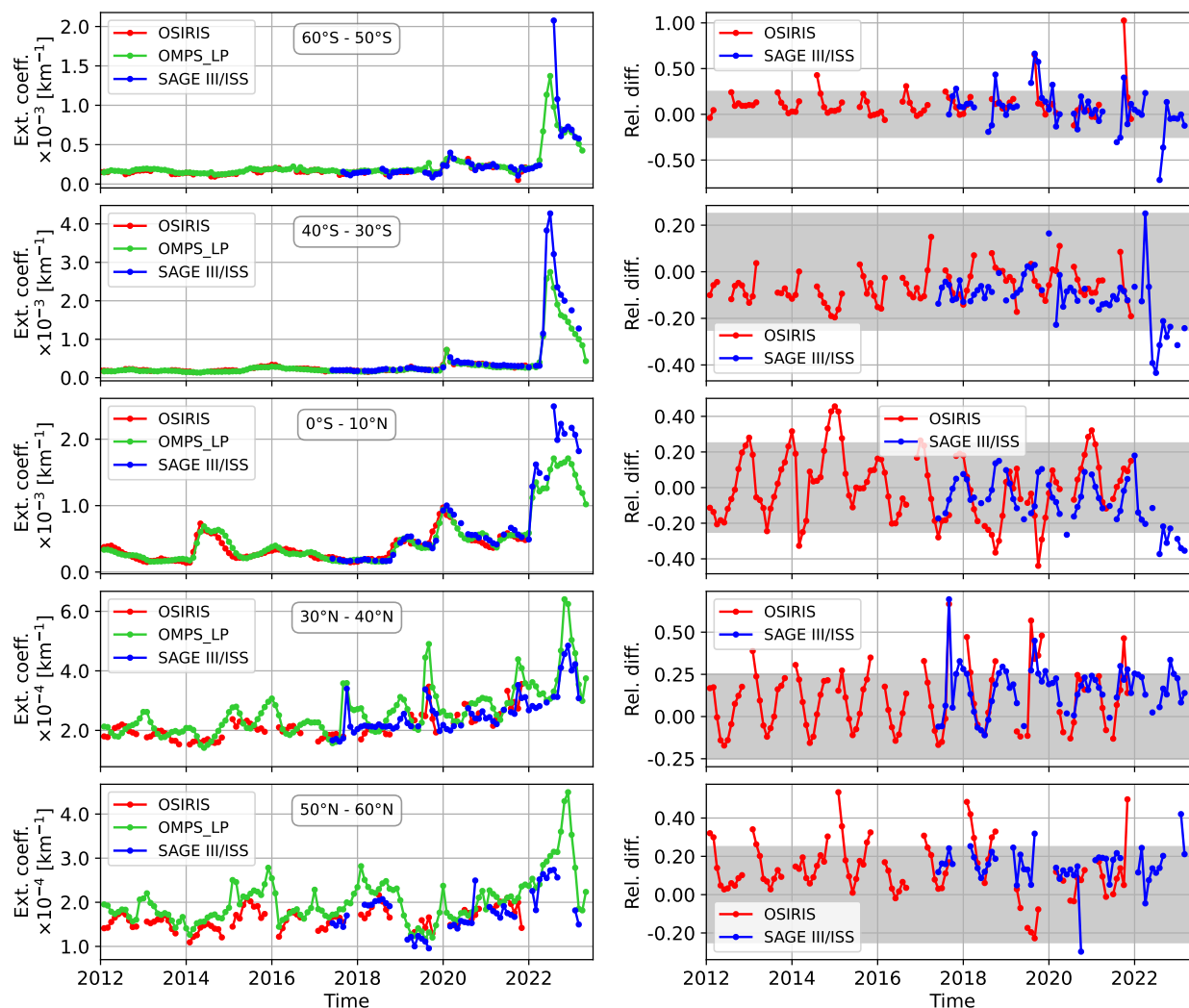
Figure 7. Comparison of monthly zonal mean aerosol extinction coefficients at 750 nm from OMPS-LP V2.1, OSIRIS and SAGE III/ISS data at an altitude of 21.5 km. Left panels: aerosol extinction coefficient time series. Right panels: relative differences. The rows show the results for different latitude bands (from top to bottom): 60°S–50°S, 40°S–30°S, 0°N–10°N, 30°N–40°N and 50°N–60°N. Grey areas mark ±25% range.

295 Ångström exponent calculated for 750 and 869 nm employing the Mie theory. The calculations were done assuming a fixed particle size distribution with the median radius of 0.08 μm and a standard deviation in the logarithmic space of 1.6 (same as used in the retrieval, see Sect. 3). This results in a constant conversion factor of 1.477 when transforming data from 869 to 750 nm. For SAGE III/ISS the aerosol extinction coefficients at 756 nm were used without any adjustment. As mentioned in

Sect.2, the University of Saskatchewan team does not recommend the usage of OSIRIS data after 2021. For this reason the
300   comparison with OSIRIS is limited to the 2012–2021 period.

Comparison of the monthly zonal mean aerosol extinction coefficients at 750 nm from OMPS-LP (V2.1), OSIRIS and SAGE III/ISS at an altitude of 21.5 km is shown in Fig. 7 for different latitude ranges. Left panels show the extinction coefficient time series while right panels depict relative differences between the respective time series and OMPS-LP data calculated as 2*(OMPS-LP - Instrument)/(OMPS-LP + Instrument). Generally, a good agreement between the results from different
305   instruments is observed with relative differences ranging mostly within ±25%, which is consistent with the results presented in Figs. 5 and 6. After the Hunga Tonga–Hunga Ha'apai eruption, the agreement between the results from OMPS-LP and SAGE III/ISS is worse in the 40°S–30°S and 0°N–10°N latitude bands. OMPS-LP values generally tend to be smaller than those from SAGE III/ISS. In the 50°N–60°N latitude band, OMPS-LP shows an increased aerosol loading in the beginning of 2023 which is not seen in SAGE III/ISS data. This might be caused by a coarser sampling of the latter instrument. In general, OMPS-LP
310   results in this latitude band are slightly higher than those from SAGE III/ISS and OSIRIS. We note, that the OMPS-LP retrievals in this latitude band have the strongest sensitivity to the aerosol particle size distribution because of a small scattering angle. In the 30°N–40°N and 0°N–10°N latitude bands, OMPS-LP data seem to show somewhat stronger seasonal cycle in comparison with both OSIRIS and SAGE III/ISS measurements and the pattern of the relative difference seems to be dominated by the seasonal cycle. The observed difference in the seasonal cycle is most probably caused by the dependence on the scattering
315   angle of the retrieval error associated with an assumption of a fixed aerosol particle size distribution. As expected, for small scattering angles as occurs at the middle and high northern latitudes for OMPS-LP observational geometry, this dependence is higher resulting in a pronounced seasonal variation of the differences between the results form OMPS-LP and those from SAGE III/ISS and OSIRIS. We note that OSIRIS instrument observes the atmosphere at a narrower range of scattering angles (60° – 120°) in comparison to that of OMPS-LP (25° – 160°).

320   To analyze the influence of seasonal variations, deseasonalized time series were investigated in addition. These were obtained by calculating absolute anomalies of the time series, i.e. by subtracting from each monthly value the mean value for this month in the considered observation period, and then adding a mean value over all months in the observational period. The comparison results for deseasonalized time series are presented in Fig. 8. The plot reveals that the differences are generally lower for the deseasonalized time series, especially in the 30°N–40°N latitude band. In contrast, the oscillating structure seen in the 0°N–
325   10°N latitude band before 2016 is not removed by the deseasonalizing procedure, indicating that these differences are most probably not related to the seasonal variations. We note, however, that due to an orbit drift, the equator crossing time of OSIRIS changes with the time. Therefore, depending on the time and latitude, either the measurement at the ascending node of the orbit or that at the descending node of both of them are made in the illuminated part of the atmosphere and their results are included into the total data product. This might influence the efficiency of the deseasonalizing procedure.

330   Figure 9 presents an overview of the relative mean differences between the OMPS-LP V2.1 and OSIRIS data as a function of the altitude and latitude. The differences were obtained by averaging all data in the 2012 – 2022 period. Below 60° latitude in the altitude range between the tropopause and about 30 km the differences between the results from both instruments are mostly within 10%. In contrast, higher differences are observed at latitudes above 60° below 20 km in the northern hemisphere
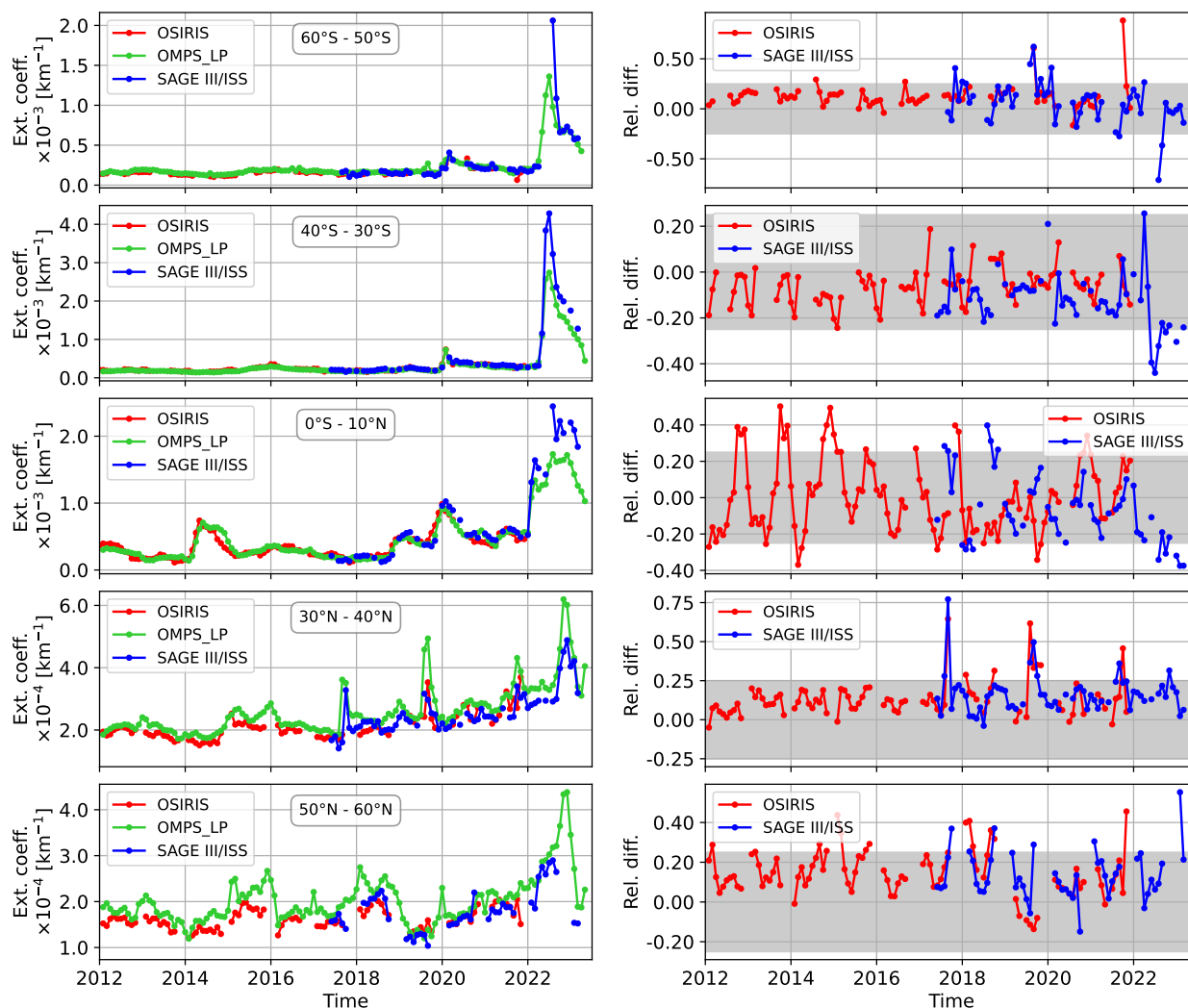
Figure 8. Same as Fig. 7 but for deseasonalized time series.

and in the whole altitude range with the maximum around 30 km in the southern hemisphere. These differences might be
335   related to the sampling issues of both instruments at high latitudes and to retrieval issues associated with a high surface albedo
and large solar zenith angles. As expected, high differences in the troposphere are observed because of a different treatment of
the clouds.

Relative mean differences between the OMPS-LP V2.1 and OSIRIS data as a function of the altitude and time are shown in
Fig. 10 for three different latitude ranges: southern mid-latitudes (60°S–20°S), tropics (20°S–20°N) and northern mid-latitudes
340   (20°N–60°N). The left panels of the plot show the results for original time series while the right panels present the differences
for deseasonalized time series. In the southern mid latitudes (top row of the plot), both datasets agree typically within 10%
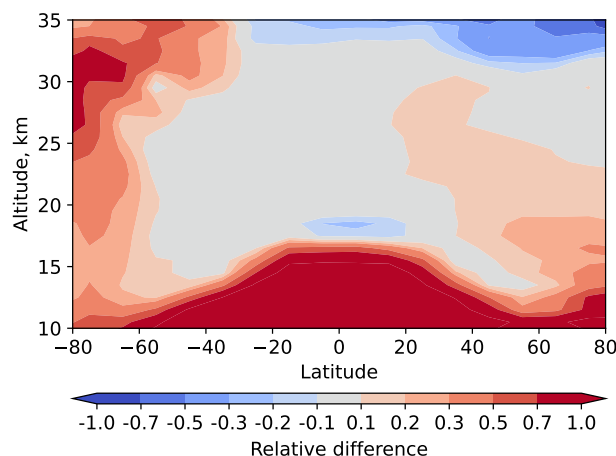
Figure 9. Comparison of zonal mean aerosol extinction coefficients at 750 nm from OMPS-LP V2.1 and OSIRIS data (2012 – 2021).

in the altitude region between 20 and 27 km. Somewhat higher differences are seen in 2020, where the stratospheric aerosol loading was increased as a results of Australian wildfires. Above 27 km and below 20 km pronounced seasonal variations are seen in the relative differences with areas of higher differences grouping around the gaps in OSIRIS observations in the austral winter months. Deseasonalizing the time series reduces the differences below 21 km to less then 20% but does not seem to have any effect above 27 km. In the tropics (middle row of the plot), the results from OMPS-LP and OSIRIS agree typically within 10-20% in the altitude region between 20 and 33 km. For the deseasonalized time series, the difference are slightly lower, however, the general picture remains almost the same. In the northern mid-latitudes (bottom row of the plot) stronger seasonal oscillations are seen in the relative differences with areas of higher differences mostly grouped around the gaps in OSIRIS observations in the boreal winter months. Somewhat higher differences are seen at the end of 2017 and the beginning of 2018, most probably associated with British Columbia forest fires. For the deseasonalized time series, the differences are largely smoothed and do not show any pronounced peaks with exception of the last months of the time series. Overall the OMPS-LP results are biased positively with respect to the OSIRIS data but the relative differences do not typically exceed 20% in the altitude range between 15 and 30 km.

7 Evolution of the aerosol plume from the Hunga Tonga–Hunga Ha'apai eruption

In this section the newly generated OMPS-LP V2.1 aerosol extinction coefficient product is used to investigate the evolution of the aerosol plume after the Hunga Tonga–Hunga Ha'apai eruption in January 2022. For this purpose a dataset of zonal mean aerosol extinction coefficients at 869 nm with an increased temporal resolution (10 days mean) was created. The altitude-time cross sections of the aerosol extinction coefficient for different latitude ranges are shown in the left panels of Fig. 11. In the tropics (top panel) the aerosol extinction coefficient raises right after the strongest eruption of the Hunga Tonga–Hunga Ha'apai occurred on January 15th, 2022 (marked by the vertical dashed line in the plots). A significant perturbation in the
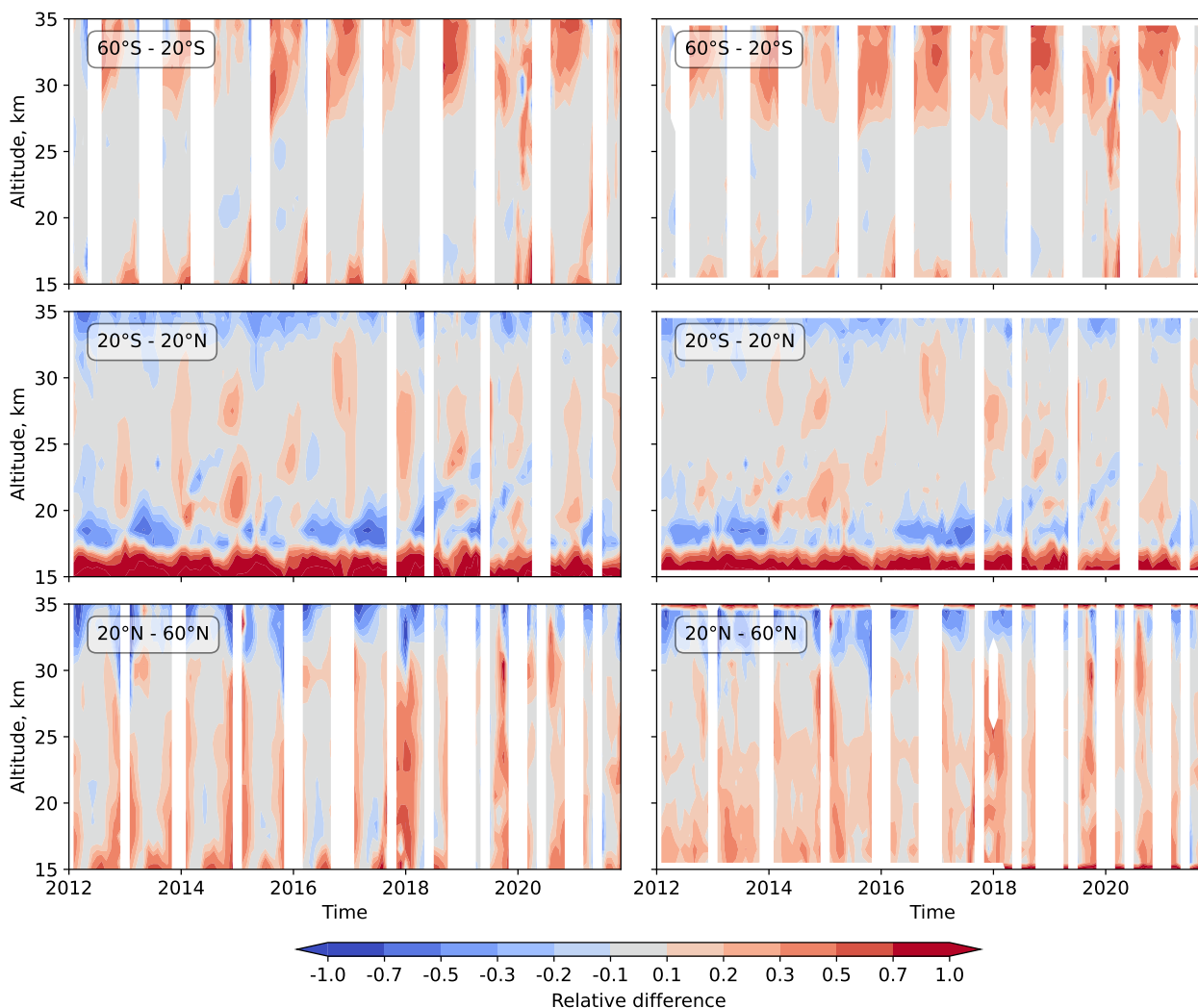
Figure 10. Relative mean differences of the monthly zonal mean aerosol extinction coefficients at 750 nm from OMPS-LP V2.1 and OSIRIS data for different latitude ranges (from top to bottom): 60°S–20°S, 20°S–20°N, 20°N–60°N. Left panels: aerosol extinction coefficient time series. Right panels: deseasonalized time series.

vertical distribution of the extinction coefficient is seen up to about 33 km. It should be noted here, that the extinction observed right after the eruption is strongly affected by the ash plume and ice clouds, which might result in high retrieval errors caused by a wrong assumption about the aerosol composition in the Mie scattering calculations of the forward model. In about one time step, i.e. 10 days, a strong increase in the aerosol extinction coefficient is observed, which is most probably caused by a creation of a significant amount of the sulfate aerosols from the sulfur injected into the stratosphere by the volcanic eruption. As reported e.g. by Legras et al. (2022), ash and ice clouds were rapidly removed within the first day after the eruption while the conversion of SO_2 to sulfates started immediately after the eruption. Thus we can assume that from the second time bin
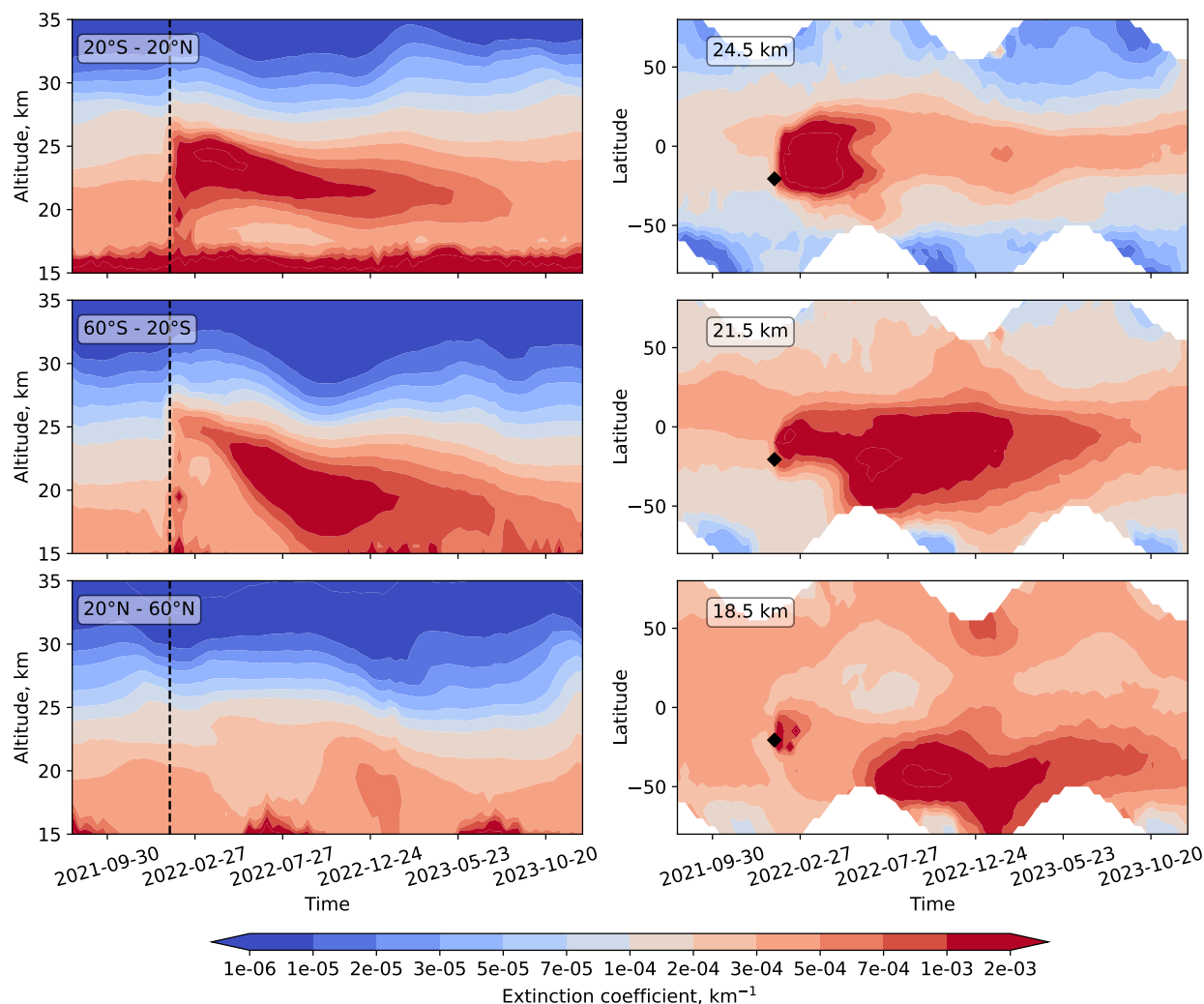
Figure 11. Evolution of the aerosol plume in different latitude bands and at different altitude levels. Left panels: 10 days zonal mean aerosol extinction coefficient at 869 nm in different latitude bands (from top to bottom): 20°S–20°N, 60°S–20°S, 20°N–60°N. The black dashed line mark the time of the strongest Hunga–Tonga eruption (January 15th, 2022). Right panels: 10 days zonal mean aerosol extinction coefficient at 869 nm at different altitude layers (from top to bottom): 24.5, 21.5, 18.5 km. The black rhombus marks the position of the Hunga Tonga–Hunga Ha'apai volcano and date of its strongest eruption. The OMPS-LP data of V2.1 were used for all plots.

after the eruption the extinction by sulfate aerosols dominates and the retrieval results are robust. It is seen from the plot that
370 the maximum of the extinction coefficient is observed between about 21 and 26 km. The plume remains stable until about the middle of April 2022 and then starts sinking. Above about 22 km the values quite rapidly relax to quasi-stationary levels, which are significantly higher than those before the eruption.

In the southern mid-latitudes, as shown in the middle left panel of the figure, a similar immediate increase of the aerosol extinction coefficient after the Hunga Tonga–Hunga Ha'apai eruption as in tropics is observed. However, rather few sulfate aerosols are observed 10-20 days after the eruption. A stronger increase in the aerosol extinction coefficient is seen only after the middle of April, when the aerosol plume in tropics started sinking and was transported into the southern mid-latitudes. Thereafter, the evolution of the plume was quite similar to that in the tropics. The plume was sinking and the values near the upper boundary of the plume quite rapidly relaxed to quasi-stationary elevated values. In the northern mid-latitudes, as shown in the bottom left panel, no instantaneous response to the Hunga Tonga–Hunga Ha'apai eruption is observed. Elevated values are observed at lower altitudes since November 2022, which are most probably caused by the transport of the Hunga Tonga–Hunga Ha'apai aerosols from the tropics. As discussed below, this statement is confirmed by the evolution of the aerosol plume observed in the latitude-time cross section plot at 21.5 km (right middle panel).

In the right panels of Fig. 11, the latitude-time cross sections of the aerosol extinction coefficient for different altitudes are shown. The latitude of the Hunga Tonga–Hunga Ha'apai volcano and the date of its strongest eruption are marked by the black rhombus. At 24.5 km (top panel), large amounts of the aerosols were created about 10 days after the eruption. The strongly elevated aerosol plume formed over the entire tropical region and partially penetrated to the southern sub-tropics. In the first four months after the eruption, the plume did not extend much in the latitudinal direction and resided mainly in the tropical region. Thereafter, a propagation of the aerosol plume to the southern mid-latitudes is observed. From June 2022, the aerosol extinction coefficient started rapidly to decrease reaching a quasi-stationary elevated level at the end of July. In spring 2023, the plume starts disapearing in the southern sub-tropics and mid-latitudes but remains stable until the end of the analyzed record (December 2023) in the tropics.

At 21.5 km (middle panel), the aerosol plume was localized in tropics within the first three months after the eruption. In May 2022, the plume rapidly propagated southwards and spread over the entire southern mid-latitudes. No propagation to the northern extratropics is seen until October 2022. Thereafter, the plume spread to the northern hemisphere.

At 18.5 km (bottom panel), a strong increase of the extinction is seen right after the eruption. Elevated values can only be observed until the end of March, before the concentration fell back to the pre-eruption level. From the beginning of June 2022, the high aerosol amounts, which propagated to the southern mid-latitudes from tropic at around 21.5 km altitude, sank to 18.5 km leading to a strong increase of the aerosol extinction in the almost entire southern hemisphere. These increased values resided at this altitude until May 2023. Thereafte a relaxation process is observed. At the end of the analyzed period (December 2023) some increase in the aerosol extinction coefficient is still observed. In the northern hemisphere, increased values of the aerosol extinction coefficient are observed at the end of 2022 and the beginning of 2023. It is, however, unclear whether these values are related to the Hunga Tonga–Hunga Ha'apai eruption plume.

8 Conclusions

In this study we have introduced a new retrieval algorithm developed to obtain vertical distributions of the aerosol extinction coefficient from limb-scatter measurements of the OMPS-LP instrument. The main change with respect to the algorithms

used by other scientific groups as well as with respect to the previous version of the University of Bremen retrieval is the normalization of the limb measurements by the solar irradince rather than by a limb measurements at an upper tangent height. As normalizing to the solar irradiance increases the sensitivity of the retrieval to the reflectance of the underlying scene, an optimized scheme to derive the effective Lambertian surface albedo has been implemented.

410   The employed normalization approach makes the retrieval results from OMPS-LP V2.1 algorithm almost independent on the prior profile of the aerosol extinction coefficient used in the retrieval. In contrast, an adequate knowledge of the aerosol extinction at altitudes around the normalization tangent height is crucial for algorithms using the normalization to a limb measurement at an upper tangent height. Furthermore, as the quality of limb measurements decreases with increasing tangent height and the influence of the stray light increases, skipping the normalization to an upper tangent height enables us to extend

415   the vertical range of the retrieval to 8.5 - 48 km in comparison with 12.5 - 37.5 km retrieval range of the previous version of the University of Bremen retrieval, published by Malinina et al. (2021). This makes the retrieval applicable to the scenes with high aerosol plume elevation, as it was the case after the Hunga Tonga–Hunga Ha'apai eruption in January 2022.

The new dataset of the OMPS-LP aerosol extinction coefficient V2.1 covering the period from February 2012 to December 2023 was verified using the data from the solar occultation SAGE III/ISS and limb-scatter OSIRIS instruments. Comparison of

420   the newly generated OMPS-LP V2.1 data product with that of SAGE III/ISS shows a good overall agreement within typically 25% between 15 and 30 km. Similarly, the comparison with OSIRIS data generally shows a good agreement of the temporal behavior and values. Within strong aerosol plumes, larger disagreement between the data from different instruments (OMPS-LP, OSIRIS, SAGE III/ISS) were identified. This is most probably related to the assumption about the aerosol particle size distribution used in the limb-scatter retrievals (OMPS-LP and OSIRIS), which was originally selected for background aerosol

425   conditions and might be sub-optimal for strong volcanic eruption conditions.

The OMPS-LP V2.1 aerosol extinction coefficient dataset was used to investigate the evolution of the aerosol plume after the Hunga Tonga–Hunga Ha'apai eruption. The perturbation of the aerosol layer is seen up to the altitude of about 33 km. A strong increase in the aerosol loading is seen up to the altitude of 27 km. About two weeks after the eruption the maximum of the aerosol absorption is seen in tropics between 21 and 26 km altitude. About 4 months after the eruption, the aerosol plume

430   started rapidly sinking. At higher altitudes (23 -25 km) the plume mainly resided in tropics, while at lower altitudes (around 18 km) the aerosol was transported southwards and spread over almost the entire southern hemisphere. At higher altitudes the relaxation already started, but at the end of the analyzed period (December 2023) the aerosol level in tropics still remained elevated in comparison to the pre-eruption level.

The OMPS-LP V2.1 aerosol extinction coefficient dataset described in this manuscript is available for the scientific commu-

435   nity via the web page of the University of Bremen (see data availability section below).

Data availability.   The OMPS-LP V2.1 aerosol extinction coefficient of IUP Bremen is available at https://www.iup.uni-bremen.de/DataRequest

Author contributions. AR developed the OMPS-LP V2.1 retrieval algorithm, generated the data set, evaluated the results and written the initial text of the manuscript. CP participated in the algorithm developments and made initial evaluation. CA prepared tools for an initial processing of OMPS-LP Level-1 data, KB provided access to all necessary Level-1 and Level-2 data. AB and LR provided Level-2 OSIRIS data and support on their usage. EM developed OMPS-LP V1.0.9 data set and provided the data for the comparison. JB did an overall scientific supervision of the study. All authors contributed to the discussion and improvement of the initial manuscript.

Competing interests. The authors declare that they have no conflict of interest.

Acknowledgements. This study was funded in parts by the European Space Agency (ESA) via CREST project, by the German Research Foundation (DFG) via the Research Unit VolImpact (grant no. FOR2820), and by the University and State of Bremen. The authors gratefully acknowledge the computing time granted by the Resource Allocation Board and provided on the supercomputer Lise and Emmy at NHR@ZIB and NHR@Göttingen as part of the NHR infrastructure. The calculations for this research were conducted with computing resources under the project hbk00098.

References

Bingen, C., Fussen, D., and Vanhellemont, F.: A global climatology of stratospheric aerosol size distribution parameters derived from SAGE II data over the period 1984–2000: 2. Reference data, Journal of Geophysical Research: Atmospheres, 109, https://doi.org/https://doi.org/10.1029/2003JD003511, 2004.

Bourassa, A. E., Degenstein, D. A., and Llewellyn, E. J.: Retrieval of stratospheric aerosol size information from OSIRIS limb scattered sunlight spectra, Atmospheric Chemistry and Physics, 8, 6375–6380, https://doi.org/10.5194/acp-8-6375-2008, 2008.

Bourassa, A. E., Rieger, L. A., Lloyd, N. D., and Degenstein, D. A.: Odin-OSIRIS stratospheric aerosol data product and SAGE III intercomparison, Atmos. Chem. Phys., 12, 605–614, 2012.

Bourassa, A. E., Zawada, D. J., Rieger, L. A., Warnock, T. W., Toohey, M., and Degenstein, D. A.: Tomographic Retrievals of Hunga Tonga-Hunga Ha'apai Volcanic Aerosol, Geophysical Research Letters, 50, e2022GL101978, https://doi.org/https://doi.org/10.1029/2022GL101978, 2023.

Bovensmann, H., Burrows, J., Buchwitz, M., Frerick, J., Noël, S., Rozanov, V., Chance, K., and Goede, A.: SCIAMACHY: Mission objectives and measurement modes, J. Atmos. Sci., 56, 127–150, 1999.

Burrows, J., Hölzle, E., Goede, A., Visser, H., and Fricke, W.: SCIAMACHY-scanning imaging absorption spectrometer for atmospheric chartography, Acta Astronautica, 35, 445–451, https://doi.org/https://doi.org/10.1016/0094-5765(94)00278-T, earth Observation, 1995.

Carr, J. L., Horváth, A., Wu, D. L., and Friberg, M. D.: Stereo Plume Height and Motion Retrievals for the Record-Setting Hunga Tonga-Hunga Ha'apai Eruption of 15 January 2022, Geophysical Research Letters, 49, e2022GL098131, https://doi.org/https://doi.org/10.1029/2022GL098131, e2022GL098131 2022GL098131, 2022.

Chu, W. P., McCormick, M. P., Zawodny, J. M., and III, L. E. M.: Stratospheric aerosol and gas experiment III, in: Earth Observing Systems II, edited by Barnes, W. L., vol. 3117, pp. 11 – 18, International Society for Optics and Photonics, SPIE, https://doi.org/10.1117/12.283815, 1997.

Deshler, T.: A review of global stratospheric aerosol: Measurements, importance, life cycle, and local stratospheric aerosol, Atmospheric Research, 90, 223–232, https://doi.org/https://doi.org/10.1016/j.atmosres.2008.03.016, 17th International Conference on Nucleation and Atmospheric Aerosols, 2008.

Evan, S., Brioude, J., Rosenlof, K. H., Gao, R.-S., Portmann, R. W., Zhu, Y., Volkamer, R., Lee, C. F., Metzger, J.-M., Lamy, K., Walter, P., Alvarez, S. L., Flynn, J. H., Asher, E., Todt, M., Davis, S. M., Thornberry, T., Vömel, H., Wienhold, F. G., Stauffer, R. M., Millán, L., Santee, M. L., Froidevaux, L., and Read, W. G.: Rapid ozone depletion after humidification of the stratosphere by the Hunga Tonga Eruption, Science, 382, eadg2551, https://doi.org/10.1126/science.adg2551, 2023.

Flynn, L., Long, C., Wu, X., Evans, R., Beck, C., Petropavlovskikh, I., McConville, G., Yu, W., Zhang, Z., Niu, J., Beach, E., Hao, Y., Pan, C., Sen, B., Novicki, M., Zhou, S., and Seftor, C.: Performance of the ozone mapping and profiler suite (OMPS) products, J. Geophys. Res.-Atmos., 119, 6181–6195, 2014.

Fyfe, J. C., von Salzen, K., Cole, J. N. S., Gillett, N. P., and Vernier, J.-P.: Surface response to stratospheric aerosol changes in a coupled atmosphere-ocean model, Geophysical Research Letters, 40, 584–588, https://doi.org/https://doi.org/10.1002/grl.50156, 2013.

Groves, K. S. and Tuck, A. F.: Simultaneous effects of CO_2 and chlorofluoromethanes on stratospheric ozone, Nature, 280, 127–129, https://doi.org/https://doi.org/10.1038/280127a0, 1979.

Groves, K. S., Mattingly, S. R., and Tuck, A. F.: Increased atmospheric carbon dioxide and stratospheric ozone, Nature, 273, 711–715, https://doi.org/https://doi.org/10.1038/273711a0, 1978.

485   Hansen, J., Sato, M., Ruedy, R., Nazarenko, L., Lacis, A., Schmidt, G. A., Russell, G., Aleinov, I., Bauer, M., Bauer, S., Bell, N., Cairns, B., Canuto, V., Chandler, M., Cheng, Y., Del Genio, A., Faluvegi, G., Fleming, E., Friend, A., Hall, T., Jackman, C., Kelley, M., Kiang, N., Koch, D., Lean, J., Lerner, J., Lo, K., Menon, S., Miller, R., Minnis, P., Novakov, T., Oinas, V., Perlwitz, J., Perlwitz, J., Rind, D., Romanou, A., Shindell, D., Stone, P., Sun, S., Tausnev, N., Thresher, D., Wielicki, B., Wong, T., Yao, M., and Zhang, S.: Efficacy of climate forcings, Journal of Geophysical Research: Atmospheres, 110, https://doi.org/https://doi.org/10.1029/2005JD005776, 2005.

490   Khodri, M., Izumo, T., Vialard, J., Janicot, S., Cassou, C., Lengaigne, M., Mignot, J., Gastineau, G., Guilyardi, E., Lebas, N., Robock, A., and McPhaden, M. J.: Tropical explosive volcanic eruptions can trigger El Niño by cooling tropical Africa, Nature Communications, 8, 778, https://doi.org/10.1038/s41467-017-00755-6, 2017.

Kloss, C., Sellitto, P., Legras, B., Vernier, J.-P., Jégou, F., Venkat Ratnam, M., Suneel Kumar, B., Lakshmi Madhavan, B., and Berthet, G.: Impact of the 2018 Ambae Eruption on the Global Stratospheric Aerosol Layer and Climate, Journal of Geophysical Research:
495   Atmospheres, 125, e2020JD032 410, https://doi.org/https://doi.org/10.1029/2020JD032410, 2020.

Legras, B., Duchamp, C., Sellitto, P., Podglajen, A., Carboni, E., Siddans, R., Grooß, J.-U., Khaykin, S., and Ploeger, F.: The evolution and dynamics of the Hunga Tonga–Hunga Ha'apai sulfate aerosol plume in the stratosphere, Atmospheric Chemistry and Physics, 22, 14 957–14 970, https://doi.org/10.5194/acp-22-14957-2022, 2022.

Llewellyn, E. J., Lloyd, N. D., Degenstein, D. A., Gattinger, R. L., Petelina, S. V., Bourassa, A. E., Wiensz, J. T., Ivanov, E. V., McDade,
500   I. C., Solheim, B. H., McConnell, J. C., Haley, C. S., von Savigny, C., Sioris, C. E., McLinden, C. A., Griffioen, E., Kaminski, J., Evans, W. F., Puckrin, E., Strong, K., Wehrle, V., Hum, R. H., Kendall, D. J., Matsushita, J., Murtagh, D. P., Brohede, S., Stegman, J., Witt, G., Barnes, G., Payne, W. F., Piché, L., Smith, K., Warshaw, G., Deslauniers, D. L., Marchand, P., Richardson, E. H., King, R. A., Wevers, I., McCreath, W., Kyrölä, E., Oikarinen, L., Leppelmeier, G. W., Auvinen, H., Mégie, G., Hauchecorne, A., Lefévre, F., de La Nöe, J., Ricaud, P., Frisk, U., Sjoberg, F., von Schéele, F., and Nordh, L.: The OSIRIS instrument on the Odin spacecraft, Canadian Journal of
505   Physics, 82, 411–422, https://doi.org/10.1139/p04-005, 2004.

Malinina, E., Rozanov, A., Niemeier, U., Wallis, S., Arosio, C., Wrana, F., Timmreck, C., von Savigny, C., and Burrows, J. P.: Changes in stratospheric aerosol extinction coefficient after the 2018 Ambae eruption as seen by OMPS-LP and MAECHAM5-HAM, Atmospheric Chemistry and Physics, 21, 14 871–14 891, https://doi.org/10.5194/acp-21-14871-2021, 2021.

McCormick, M.: Sage II: An overview, Advances in Space Research, 7, 219–226, https://doi.org/https://doi.org/10.1016/0273-
510   1177(87)90151-7, 1987.

Millán, L., Santee, M. L., Lambert, A., Livesey, N. J., Werner, F., Schwartz, M. J., Pumphrey, H. C., Manney, G. L., Wang, Y., Su, H., Wu, L., Read, W. G., and Froidevaux, L.: The Hunga Tonga-Hunga Ha'apai Hydration of the Stratosphere, Geophysical Research Letters, 49, e2022GL099 381, https://doi.org/https://doi.org/10.1029/2022GL099381, e2022GL099381 2022GL099381, 2022.

Paik, S. and Min, S.-K.: Assessing the Impact of Volcanic Eruptions on Climate Extremes Using CMIP5 Models, Journal of Climate, 31,
515   5333 – 5349, https://doi.org/https://doi.org/10.1175/JCLI-D-17-0651.1, 2018.

Portmann, R. W., Solomon, S., Garcia, R. R., Thomason, L. W., Poole, L. R., and McCormick, M. P.: Role of aerosol variations in anthropogenic ozone depletion in the polar regions, Journal of Geophysical Research: Atmospheres, 101, 22 991–23 006, https://doi.org/https://doi.org/10.1029/96JD02608, 1996.

Proud, S. R., Prata, A. T., and Schmauß, S.: The January 2022 eruption of Hunga Tonga-Hunga Ha'apai volcano reached the mesosphere,
520   Science, 378, 554–557, https://doi.org/10.1126/science.abo4076, 2022.

Rault, D. F., Loughman, R., Taha, G., and Fleig, A. J.: Algorithm Theoretical Basis Document (ATBD) for the Environment Data Record (EDR) Algorithm of the Ozone Mapping and Profiler Suite (OMPS) Limb Profiler National Polar-Orbiting Operational Environmental Satellite System (NPOESS) Program, https://ozoneaq.gsfc.nasa.gov/media/docs/EDR_ATBD_baseline_version1.pdf, 2010.

Rieger, L. A., Bourassa, A. E., and Degenstein, D. A.: Merging the OSIRIS and SAGE II stratospheric aerosol records, J. Geophys. Res. Atmos., 120, 8890–8904, 2015.

Rieger, L. A., Zawada, D. J., Bourassa, A. E., and Degenstein, D. A.: A Multiwavelength Retrieval Approach for Improved OSIRIS Aerosol Extinction Retrievals, Journal of Geophysical Research: Atmospheres, 124, 7286–7307, https://doi.org/https://doi.org/10.1029/2018JD029897, 2019.

Rodgers, C. D.: Inverse methods for atmospheric sounding: Theory and practice, World Scientific, 2000.

Rozanov, A., Rozanov, V., and Burrows, J. P.: Combined differential-integral approach for the radiation field computation in a spherical shell atmosphere: Non-limb geometry, J. Geophys. Res., 102, 22 937–22 942, 2000.

Rozanov, A., Rozanov, V., and Burrows, J. P.: A numerical radiative transfer model for a spherical planetary atmosphere: Combined differential–integral approach involving the Picard iterative approximation, J. Quant. Spectrosc. Radiat. Transfer, 69, 491–512, 2001.

Rozanov, A., Kühl, S., Doicu, A., McLinden, C., Puķīte, J., Bovensmann, H., Burrows, J. P., Deutschmann, T., Dorf, M., Goutail, F., Grunow, K., Hendrick, F., von Hobe, M., Hrechanyy, S., Lichtenberg, G., Pfeilsticker, K., Pommereau, J. P., Van Roozendael, M., Stroh, F., and Wagner, T.: BrO vertical distributions from SCIAMACHY limb measurements: comparison of algorithms and retrieval results, Atmospheric Measurement Techniques, 4, 1319–1359, https://doi.org/10.5194/amt-4-1319-2011, 2011.

Solomon, S., Garcia, R. R., Sherwood, R. F., and Wuebbles, D. J.: On the depletion of Antarctic ozone, Nature, 321, 755–758, https://doi.org/https://doi.org/10.1038/321755a0, 1986.

Solomon, S., Daniel, J. S., Neely, R. R., Vernier, J.-P., Dutton, E. G., and Thomason, L. W.: The Persistently Variable "Background" Stratospheric Aerosol Layer and Global Climate Change, Science, 333, 866–870, https://doi.org/10.1126/science.1206027, 2011.

Solomon, S., Stone, K., Yu, P., Murphy, D. M., Kinnison, D., Ravishankara, A. R., and Wang, P.: Chlorine activation and enhanced ozone depletion induced by wildfire aerosol, Nature, 615, 259–264, https://doi.org/10.1038/s41586-022-05683-0, 2023.

Taha, G., Loughman, R., Zhu, T., Thomason, L., Kar, J., Rieger, L., and Bourassa, A.: OMPS LP Version 2.0 multi-wavelength aerosol extinction coefficient retrieval algorithm, Atmospheric Measurement Techniques, 14, 1015–1036, https://doi.org/10.5194/amt-14-1015-2021, 2021.

Tritscher, I., Pitts, M. C., Poole, L. R., Alexander, S. P., Cairo, F., Chipperfield, M. P., Grooß, J.-U., Höpfner, M., Lambert, A., Luo, B., Molleker, S., Orr, A., Salawitch, R., Snels, M., Spang, R., Woiwode, W., and Peter, T.: Polar Stratospheric Clouds: Satellite Observations, Processes, and Role in Ozone Depletion, Reviews of Geophysics, 59, e2020RG000 702, https://doi.org/https://doi.org/10.1029/2020RG000702, 2021.

von Savigny, C., Ernst, F., Rozanov, A., Hommel, R., Eichmann, K.-U., Rozanov, V., Burrows, J. P., and Thomason, L. W.: Improved stratospheric aerosol extinction profiles from SCIAMACHY: validation and sample results, Atmospheric Measurement Techniques, 8, 5223–5235, https://doi.org/10.5194/amt-8-5223-2015, 2015.

Winker, D. M., Vaughan, M. A., Omar, A., Hu, Y., Powell, K. A., Liu, Z., Hunt, W. H., and Young, S. A.: Overview of the CALIPSO Mission and CALIOP Data Processing Algorithms, Journal of Atmospheric and Oceanic Technology, 26, 2310 – 2323, https://doi.org/https://doi.org/10.1175/2009JTECHA1281.1, 2009.

Young, S. A., Vaughan, M. A., Kuehn, R. E., and Winker, D. M.: The Retrieval of Profiles of Particulate Extinction from Cloud-Aerosol Lidar and Infrared Pathfinder Satellite Observations (CALIPSO) Data: Uncertainty and Error Sensitivity Analyses, Journal of Atmospheric and Oceanic Technology, 30, 395 – 428, https://doi.org/https://doi.org/10.1175/JTECH-D-12-00046.1, 2013.

560   Young, S. A., Vaughan, M. A., Garnier, A., Tackett, J. L., Lambeth, J. D., and Powell, K. A.: Extinction and optical depth retrievals for CALIPSO's Version 4 data release, Atmospheric Measurement Techniques, 11, 5701–5727, https://doi.org/10.5194/amt-11-5701-2018, 2018.